Molecular Ferroelectric-Based Flexible Sensors Exhibiting Supersensitivity and Multimodal Capability for Detection

Wenru Li, Changhao Li, Guangzu Zhang, Linkai Li, Kai Huang, Xuetian Gong, Chao Zhang, An Zheng, Yanxue Tang, Zhengzhi Wang, Qiaoling Tong, Wen Dong, Shenglin Jiang, Sulin Zhang,* and Qing Wang**

Although excellent dielectric, piezoelectric, and pyroelectric properties matched with or even surpassing those of ferroelectric ceramics have been recently discovered in molecular ferroelectrics, their successful applications in devices are scarce. The fracture proneness of molecular ferroelectrics under mechanical loading precludes their applications as flexible sensors in bulk crystalline form. Here, self-powered flexible mechanical sensors prepared from the facile deposition of molecular ferroelectric $[C(NH_2)_3]ClO_4$ onto a porous polyurethane (PU) matrix are reported. $[C(NH_2)_3]ClO_4$-PU is capable of detecting pressure of 3 Pa and strain of 1% that are hardly accessible by the state-of-the-art piezoelectric, triboelectric, and piezoresistive sensors, and presents the ability of sensing multimodal mechanical forces including compression, stretching, bending, shearing, and twisting with high cyclic stability. This scaling analysis corroborated with computational modeling provides detailed insights into the electro-mechanical coupling and establishes rules of engineering design and optimization for the hybrid sponges. Demonstrative applications of the $[C(NH_2)_3]ClO_4$-PU array suggest potential uses in interactive electronics and robotic systems.

1. Introduction

Molecular ferroelectrics are inorganic–organic hybrids consisting of organic molecular groups and inorganic atomic framework, in which ferroelectricity arises from the asymmetry of their lattice structures and relative displacement of ions/polar groups.[1–4] Although ferroelectricity was discovered in molecular materials (Rochelle salt, $KNaC_4H_4O_6{\cdot}4H_2O$) in 1920,[5] the field has been long dominated by perovskite oxides represented by barium titanate (BTO) and lead zirconate titanate (PZT) and synthetic polymers including poly(vinylidene fluoride) and polyamides, which have led to a wide range of industrial applications such as film capacitors, transducers, actuators, sensors, and memories.[6–12] The research activities on molecular ferroelectrics are being rejuvenated owing to the most recent breakthroughs such as the discovery of the molecular crystals with large spontaneous polarization (e.g., P_S = 22 μC cm^{-2}) close to that of BTO (P_S = 26 μC cm^{-2}) and higher transition temperatures than that of BTO (e.g., T_0 = 448 K vs 390 K),[13] the ultrafast polarization switching in thin films based on biaxial molecular ferroelectrics,[14] and the pyroelectric figures-of-merit outperforming the current ferroelectric

---

W. Li, G. Zhang, L. Li, X. Gong, C. Zhang, A. Zheng, Q. Tong, W. Dong, S. Jiang
School of Optical and Electronic Information, and Wuhan National Laboratory for Optoelectronics
Huazhong University of Science and Technology
Wuhan, Hubei 430074, China
E-mail: zhanggz@hust.edu.cn

C. Li, S. Zhang
Department of Engineering Science and Mechanics
The Pennsylvania State University
University Park, PA 16802, USA
E-mail: suz10@psu.edu

K. Huang, Z. Wang
Department of Engineering Mechanics
School of Civil Engineering
Wuhan University
Wuhan 430072, China

Y. Tang
Key Laboratory of Optoelectronic Material and Device
Department of Physics
Shanghai Normal University
Shanghai 200234, China

Z. Wang
State Key Laboratory of Water Resources and Hydropower Engineering Science
Wuhan University
Wuhan 430072, China

Q. Wang
Department of Materials Science and Engineering
The Pennsylvania State University
University Park, PA 16802, USA
E-mail: wang@matse.psu.edu

The ORCID identification number(s) for the author(s) of this article can be found under https://doi.org/10.1002/adma.202104107.

DOI: 10.1002/adma.202104107

materials.[15] Compared to inorganic ferroelectrics, molecular ferroelectrics enjoy inherent advantages including light weight, structural tunability, and easy processability.[1,4,13–17] However, to the best of our knowledge, there are almost no reports on the exploration of molecular ferroelectrics for device applications even though a series of exciting dielectric, piezoelectric, and pyroelectric properties are revealed in molecular ferroelectrics.

The intrinsic piezo- and pyro-electric properties of ferroelectric materials enable a wide range of sensing applications.[18–20] In particular, much attention has recently been paid to the development of flexible pressure sensors with the pressure range targeting daily human activities for electronic skins (E-skins), human–machine interfaces, and healthcare monitoring.[21–26] The flexible sensors based on the piezoelectric transduction mechanism offer an efficient route to convert mechanical stimuli into electrical signals for sensing without external power supply, which greatly enhances the adaptability, mobility, and durability of the sensors.[23,24,27–29] Since bulk materials have a relatively high modulus and are more resistant to deformation under pressure, introducing microstructures such as, micro-pyramid arrays,[30] wrinkles,[31] micro-domes,[32] micro-pillar arrays,[33] and other cone-like patterns[34] into sensory materials has been shown to effectively improve the mechanical–electrical energy coupling and the sensitivity of pressure sensors. For example, the mechanics analyses reveal that the 3D interconnected architecture of the ferroelectric sponge renders highly effective load transfer and exhibits significantly improved piezoelectricity as compared to the corresponding low-dimensional structures.[35–38] Although the sophisticated microstructures have greatly contributed to improving the performances of piezoelectric sensors, the possibility to fabricate such devices on flexible substrates by means of simple and low-cost technologies becomes problematic. Contrary to ferroelectric ceramics and polymers, molecular ferroelectrics offer the benefits that they crystallize directly from solution and can be deposited on a variety of substrates at ambient conditions.

Here, we present the first example of flexible mechanical sensors based on the deposition of guanidinium perchlorate ($[C(NH_2)_3]ClO_4$) onto a polyurethane (PU) sponge. The resulting $[C(NH_2)_3]ClO_4$-PU hybrid material featuring a series of unique characteristic includes self-powering, high sensitivity, excellent durability, and simultaneous energy-absorption and monitoring. The high sensitivity enables $[C(NH_2)_3]ClO_4$-PU to sense a stress as small as 3 Pa (0.0013 N) and a strain of 1% that are hardly accessible by the state-of-the-art ferroelectric, triboelectric, and piezoresistive sensors. Moreover, the hybrid exhibits multimodal detection capability of mechanical signals including compression, stretching, bending, shearing, and twisting and has been assembled into the array to monitor the loading conditions of the robot hand and to recognize the shape of objects. A scaling analysis combined with finite element analysis (FEA) enables targeted design and performance optimization of such hybrid materials. It is anticipated that the ferroelectric sponge sensors would enable a large scope of potential applications ranging from energy-absorbing smart structures, conformable transducers, to electric skins.

2. Results and Discussion

2.1. Crystal Structure and Ferroelectric Property of the Molecular Ferroelectric $[C(NH_2)_3]ClO_4$

$[C(NH_2)_3]ClO_4$ is an inorganic–organic hybrid consisting of organic molecule of $[C(NH_2)_3]^+$ group and ClO_4^- inorganic atomic framework.[39] X-ray diffraction (XRD, **Figure 1**a) shows that $[C(NH_2)_3]ClO_4$ crystalizes into the space group *R3m* (trigonal point group *3m*), in which the oxygen atoms of ClO_4^- bond with the nitrogen atoms of $[C(NH_2)_3]^+$ with the hydrogen bonds to form 2D networks. As illustrated in Figure 1b, three of the four oxygen atoms are in the hydrogen bonds, while the forth atom is out of the sheet. In addition, the gravity center of the anions is situated out of the plane that parallel to the direction of [001] and pass through the cations within the sheets.[40] Therefore, the ions with opposite charges are displaced by δ along the c axis (Figure 1b), generating the parallelly ordered dipole moments and the polarization of the sheets. The polarization mechanism of $[C(NH_2)_3]ClO_4$ is thus radically different from the conventional displacive ferroelectrics whose polarization originates from the ion displacement,[7] and the ferroelectric polymers in which polarization arises from alternating $-CF_2$ and $-CH_2$ groups along the polymer chains.[6] The molecular ferroelectric crystals exhibit a macroscopic electric polarization of ~4 μC cm^{-2}, as shown in Figure S1a, Supporting Information. Below the ferroelectric-paraelectric phase transition temperature of ~177 °C (Figure S2, Supporting Information), $[C(NH_2)_3]ClO_4$ displays stable dielectric properties with a dielectric constant of 9.7 and a dielectric loss of <0.7% (Figure S1b, Supporting Information), a typical amplitude–voltage butterfly loop (Figure S3, Supporting Information), and a high piezoelectric constants of d_{33} of ~15 pC N^{-1} and d_{15} of ~13 pC N^{-1}. Although the piezoelectric constants of $[C(NH_2)_3]ClO_4$ are comparable to those of ferroelectric polymers and inferior to those of the best ferroelectric ceramics such as barium titanate (BTO) and lead zirconate titanate (PZT), its piezoelectric voltage coefficient of $g_{33} = d_{33}/\varepsilon = 170$ mV m N^{-1} (ε: the dielectric constant) is more than one order of magnitude greater than those of BTO (i.e., 11.4) and PZT (i.e., 15) owing to its low dielectric constant,[8,9] which indicates very high piezoelectric voltage responses of $[C(NH_2)_3]ClO_4$-PU hybrid.

2.2. Preparation of $[C(NH_2)_3]ClO_4$-PU Hybrid

Figure 1c and Figure S4, Supporting Information, illustrate the fabrication of the 3D interconnected molecular ferroelectric hybrid structures by immersing a PU sponge into saturated $[C(NH_2)_3]ClO_4$ aqueous solution. Upon evaporation of the solvent at room temperature, $[C(NH_2)_3]ClO_4$ crystalizes and is physically grafted onto the skeleton of the sponge, yielding $[C(NH_2)_3]ClO_4$-PU hybrid. As known to us, the fabrication process of the $[C(NH_2)_3]ClO_4$-PU hybrid is much easier than the most of reported works to achieve flexible sensing devices (Table S3, Supporting Information). $[C(NH_2)_3]ClO_4$-PU hybrid retains the crystal structure of $[C(NH_2)_3]ClO_4$ (Figure 1a) and pore structure of the original PU template with a pore size ~250 μm (Figure 1d and Figure S5, Supporting Information)

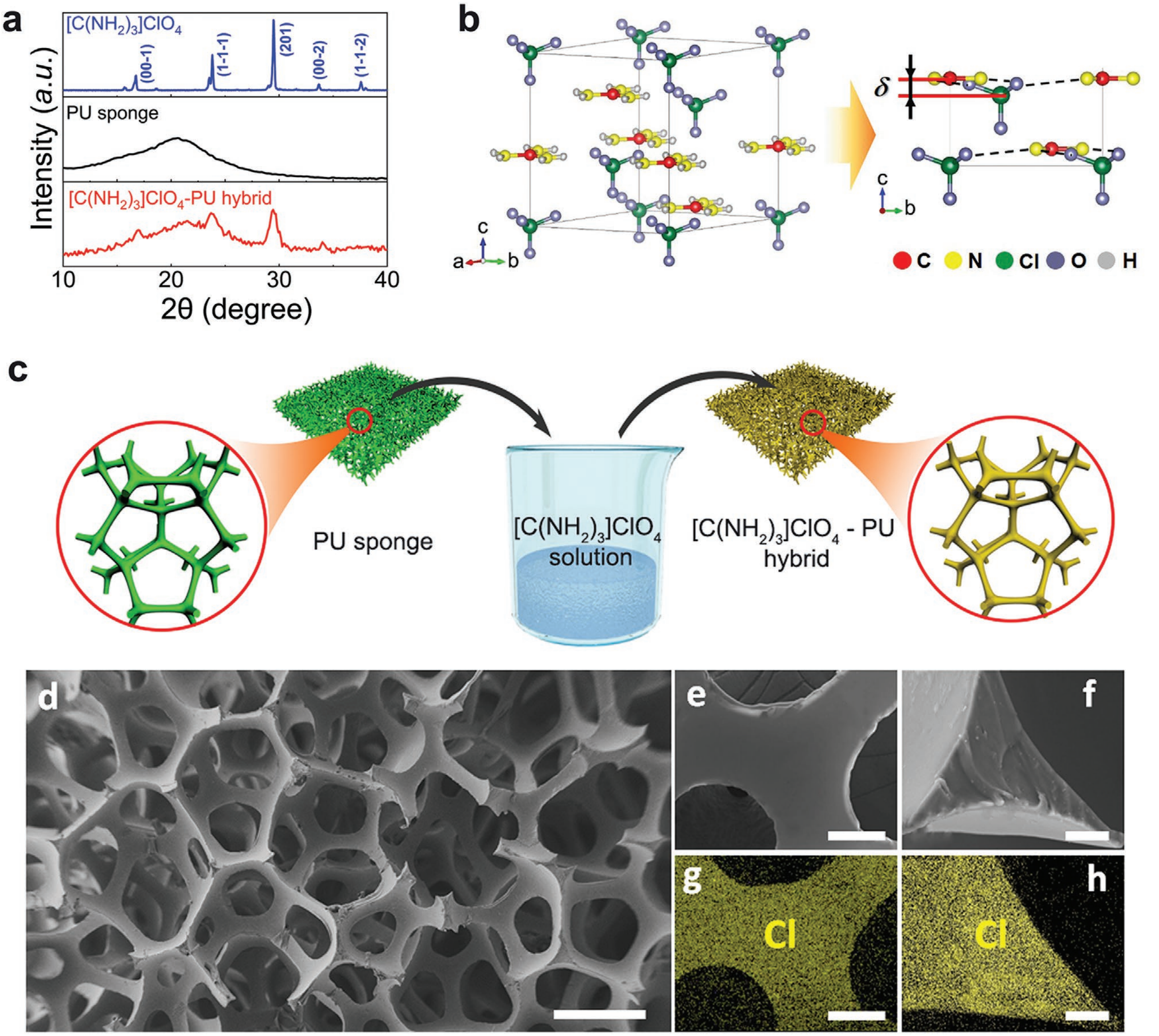

Figure 1. a) XRD patterns of $[C(NH_2)_3]ClO_4$, the PU sponge, and the $[C(NH_2)_3]ClO_4$-PU hybrid. b) Molecular structure schematic diagram of $[C(NH_2)_3]ClO_4$ from the perspective of 3D and *a*-axis. c) Schematic of fabrication process of $[C(NH_2)_3]ClO_4$-PU hybrid sponge. d) An SEM image of the 3D $[C(NH_2)_3]ClO_4$-PU hybrid. Scale bar: 300 µm. e–h) The magnified SEM image of the skeletons of $[C(NH_2)_3]ClO_4$-PU hybrid sponge and the EDS mappings of Cl element. Scale bars for (e, g), 40 µm, and scale bars for (f, h), 10 µm.

and a porosity of ~95%. The uniform dispersion of $[C(NH_2)_3]ClO_4$ crystals along the PU skeleton is evidenced by the energy dispersive spectroscopy (EDS) mapping and spectrum of Cl element (Figure 1g,h and Figure S6, Supporting Information). The overlap of the stress–strain loops of the hybrid and PU sponge suggests that the grafted $[C(NH_2)_3]ClO_4$ has a negligible impact on the mechanical properties of PU matrix and $[C(NH_2)_3]ClO_4$-PU hybrid fully retains the mechanical flexibility of original PU sponge (Figure S7, Supporting Information). The hybrid can be compressed, bended, stretched, sheared, and twisted to large deformation without fracture, demonstrating its super flexibility (Figure S8, Supporting Information).

It is worth noting that the preparation of the 3D structure of the molecular ferroelectric is a facile, low-cost, and room-temperature process and scalable as evidenced by using large PU sponge templates shown in Figure S9, Supporting Information. In stark contrast, high-temperature calcination and sintering are needed for the fabrication of 3D ferroelectric ceramics,[29,35] whereas the porous ferroelectric polymers are typically prepared by a laborious process with careful control over solvent/polymer ratio and solvent evaporation rate.[35–37,41,42]

2.3. Pressure Sensing Performance

The low-pressure regime (<10 kPa) covers intrabody pressures and the pressures created by gentle interaction with objects and is a vital range for sensor applications in E-skins, health

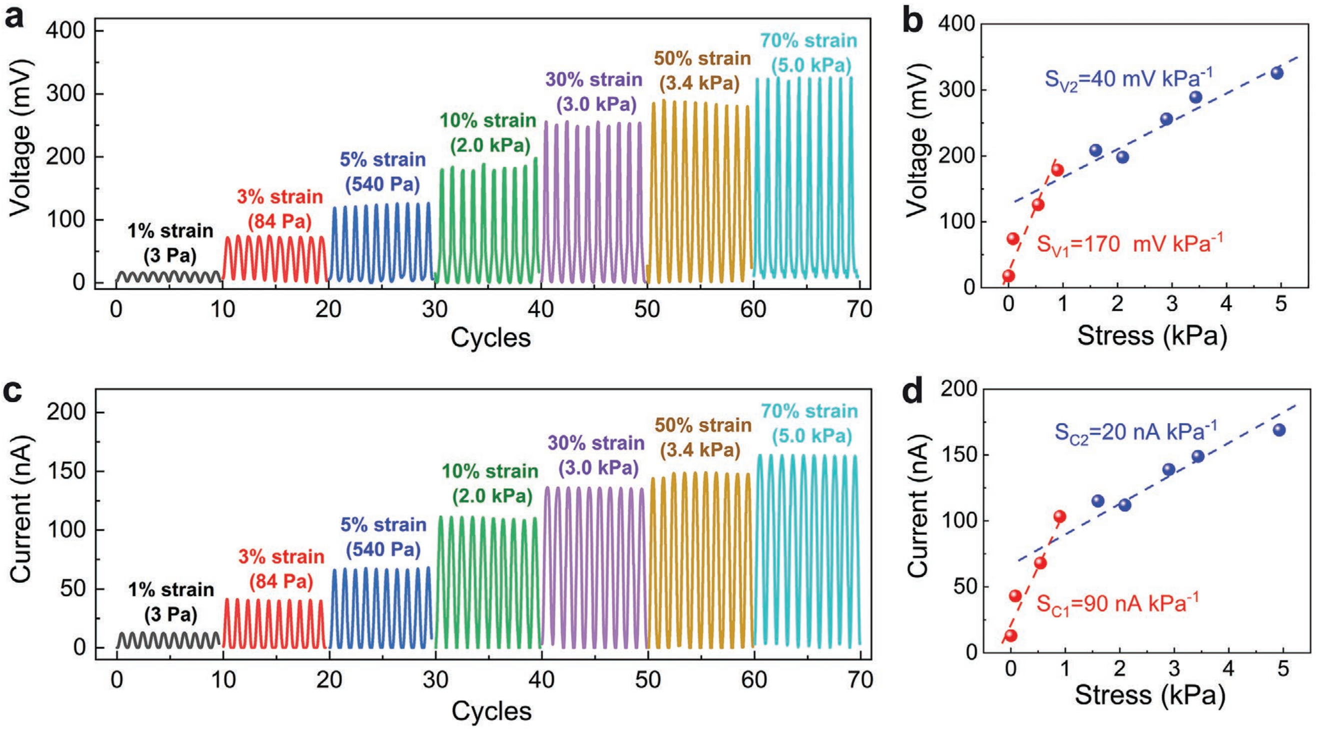

Figure 2. a,c) The piezoelectric voltage and current of the hybrid pressed with various stresses. b,d) The sensitivity of the hybrid sensor under various stresses.

care, and medical diagnostic systems.[43,44] It is found that the $[C(NH_2)_3]ClO_4$-PU hybrid displays ultra-high piezoelectric responses under subtle pressure (1 Pa to 1 kPa). As shown in **Figure 2**a,c and Figure S10a, Supporting Information, the piezoelectric voltage and current increase from 16 mV and 12 nA with 3 Pa (1% strain) to 126 mV and 68 nA under 540 Pa (5% strain). The piezoelectric voltages have also been collected with an oscilloscope and a voltmeter with different sampling rates (Figures S11 and S12, Supporting Information). The resulting sensitivities (Figure 2b,d) of 170 mV kPa^{-1} (420 mV N^{-1}) and 90 nA kPa^{-1} (215 nA N^{-1}) are among the state-of-the-art in comparison to the current pressure sensors based on the piezoresistive, piezoelectric, and triboelectric ceramics, polymers, and ceramic–polymer composites (Table S4, Supporting Information). The high sensitivity enables the 3D hybrid sponge to detect a stress as low as 3 Pa (0.0013 N) and strain of 1%, which are hardly accessible in the current piezo-resistive, triboelectric, and piezoelectric sensors. In the intermediate range around 2 kPa, due to the softening effect caused by the buckling of the slender beams in the sponge sensor under compression[45,46] when strain gradually increases, the stress temporarily decreases (Figure S7, Supporting Information). In this intermediate range (~1–2 kPa), the hybrid sensor shows a sensitivity of 44 mV kPa^{-1} and 25 nA kPa^{-1} (Figure S13, Supporting Information). As shown in Figure 2, the piezoelectric voltages and currents of the hybrid increase with the stress and strain, which gives rise to high sensitivities of 40 mV kPa^{-1} (110 mV N^{-1}) and 20 nA kPa^{-1} (52 nA N^{-1}) over a range from 2 kPa (10% strain) to 5 kPa (70% strain). It is noted that no piezoelectric response has been observed in pure PU sponge and the $[C(NH_2)_3]ClO_4$-PU hybrid without poling (Figure S14, Supporting Information), confirming that the signals shown in Figure 2 originate from the piezoelectric effect of $[C(NH_2)_3]ClO_4$.

Compared to the pressure ranges of 10 Pa to 1 kPa and 100 Pa to 10 kPa of the conventional piezoelectric sensors, the $[C(NH_2)_3]ClO_4$-PU hybrid features a much lower detection limit with higher sensitivities. The high sensitivity over a relatively wide operation range enables the hybrid sponge to respond efficiently to both very small force stimulus such as the drop of millet and large mechanical strike, e.g., the drop of iron block (Video S1, Notes S1 and S2, and Figures S15 and S16, Supporting Information).

The high performance of $[C(NH_2)_3]ClO_4$-PU hybrid was quantitatively rationalized by the FEA (**Figure 3** and Note S1, Supporting Information). Without loss of generality, the morphology of the 3D interconnected hybrid was simplified as an array of the so-called "Weaire-Phean" structure,[47] which has been widely used in modeling the microstructure of sponges (Figure 3b). In our model, we treated the hybrid as an isotropic elastic material with the polarization direction parallel to the thickness direction of the sensor. Detailed mechanical constant (Y_{ij}), dielectric constant (ε_{ij}), and piezoelectric constant (d_{ij}) used in our simulation are listed in Table S1, Supporting Information. As shown in Figure 3a, a representative cell with $1 \times 1 \times 1$ mm^3 was created to reduce the complexity of our model and capture the micromechanics behaviors. Voltage distribution of a unit cell (Figure 3b) can be obtained by solving coupled mechanical equilibrium equation $\nabla \cdot \boldsymbol{\sigma} = 0$ and electrostatic equilibrium equation $\nabla \cdot \mathbf{D} = 0$ with periodic boundary conditions, where $\mathbf{D}$ and $\boldsymbol{\sigma}$ are the electrical displacement vector and

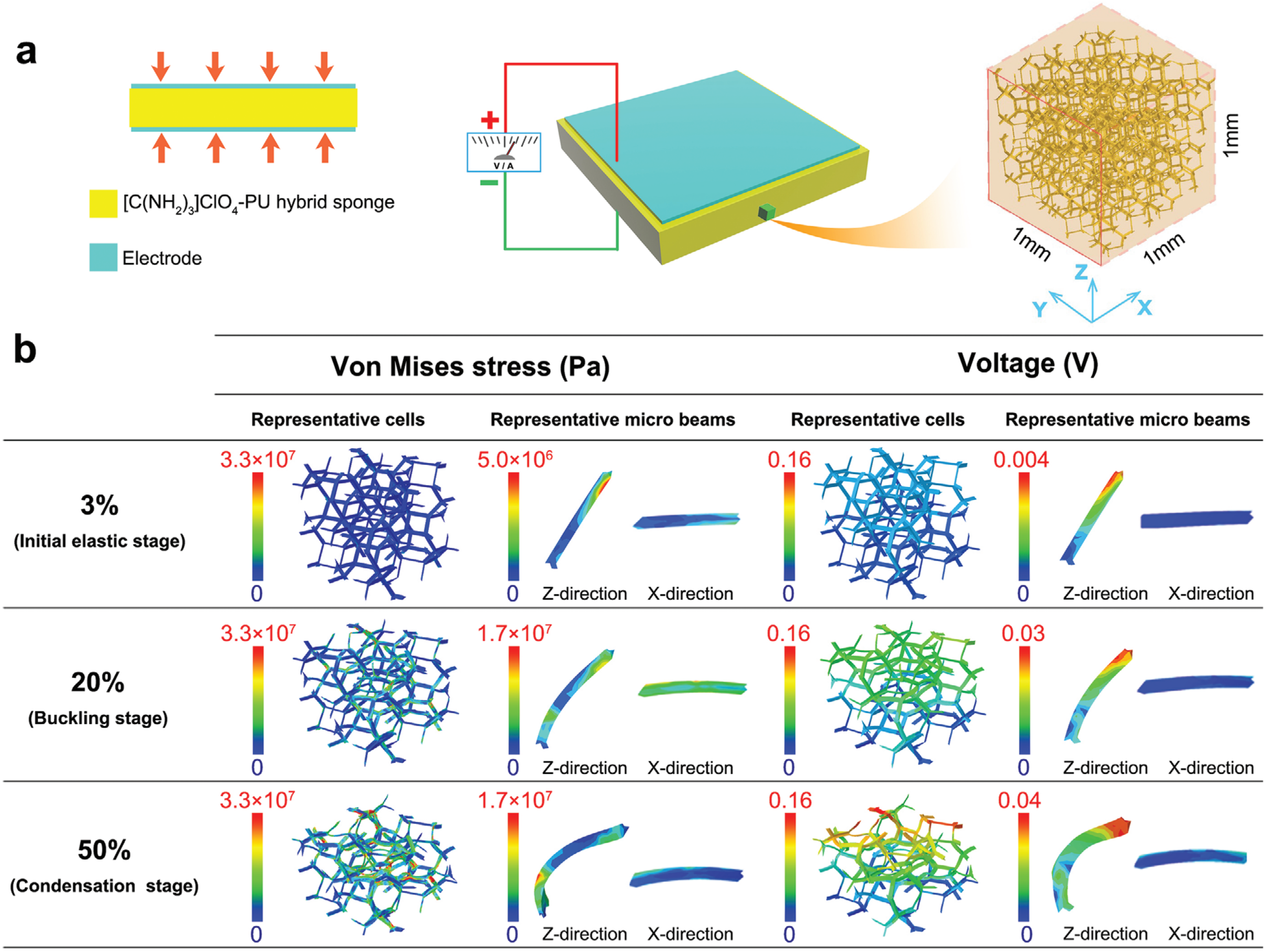

Figure 3. a) Schematic of $[C(NH_2)_3]ClO_4$-PU hybrid sponge sensor and finite element model of the representative volume of the hybrid. b) The FEA results of Von Mises stresses and piezoelectric voltages for $[C(NH_2)_3]ClO_4$-PU hybrid sponge under different deformation stages (3%, 20%, and 50% compressive strain, respectively) are expressed in different resolution.

stress tensor, respectively. Our modeling results agree with the scaling analysis and the experimental data regarding the origin of the high sensitivity of the piezoelectric sponges: the ultrahigh porosity of the 3D sponge structure amplifies the applied stress, with the estimated amplification factor α^{-1} (Note S2, Figure S18, Supporting Information). For example, the stress amplification factor can reach up to ~20 for the sponge samples with a porosity of ~95% (Figure S18, Supporting Information), corresponding to the high sensitivity of 170 mV kPa^{-1} and 90 nA kPa^{-1}. More modeling details are elaborated in Note S2, Supporting Information.

As analyzed in Figure 3 and Figures S17 and S19a–d, Supporting Information, for a relatively small compressive strain (<~10%), the hybrid exhibits strain-stiffening effect due to the condensation of unstable boundary "needling" at the microstructure level. Then, there is a linear stage following in the stress–strain curve (Figure S20a, Supporting Information). With the compressive stress increasing, the microstructure in the hybrid gradually buckles, which is corresponding to the nearly zero-stiffness portion of the mechanical response (Figure S20a, Supporting Information). When the compressive strain exceeds 40%, the buckled microstructure starts to contact with each other. In this stage, the hybrid behaves more like solid rather than porous material, because the microstructure densifies and the stiffness rapidly increases.

The contribution of the microbeams to the electrical potential is orientation dependent. For a microbeam aligning along the polarization direction (also the loading direction), compression effectively transfers to the microbeam, leading to large piezoelectric response, which is corresponding to the *z*-direction micro-beam in Figure 3b. In contrast, a microbeam perpendicular to the polarization direction is stretched due to the Poisson's effect, which also generates a potential in the thickness direction. However, this is a secondary effect and negligible (Figure 3b). For a microbeam with arbitrary orientations, it experiences a complex stress state, possibly a superposition of pressing, bending, and shearing. The electrical potential generated by these microbeams should fall in the range of those of the two special cases: perpendicular and parallel to the polarization direction. As the compressive load increases, the vertical beams buckle and their polarization direction misaligns with the loading direction (Figure 3b), then the piezoelectricity decreases. As the horizontally oriented beam is subjected to tensile loading, it hardly buckles. Thus, the vertical beams contribute mostly to the electrical field, while the horizontal beams to the mechanical stability. An arbitrarily oriented microbeam contributes to both in an intermediate fashion. Our FEA shows that the calculated voltages responding to the pressing strain are in good agreement with the experimental data (Figure S10a, Supporting Information).

2.4. Multimode Detection of Mechanical Stimuli

In addition to compression, $[C(NH_2)_3]ClO_4$-PU hybrid is effective in sensing stretching, shearing, bending, and twisting (Figures S21–S24, Supporting Information). As shown in Figure S10b–e and Figure S25, Supporting Information, excellent sensitivities of 8–20 and 0.7 mV kPa^{-1} are achieved in stretching and shearing (Figure S10b–e, Supporting Information), respectively. While there are a few reports on mechanical sensors capable of identifying compression and shearing forces, none of them possesses the capability of simultaneous detection of multimode mechanical forces including stretching, bending, and twisting.

To distinguish the mechanical stimuli from different directions, we build a 4 × 4 proof-of-concept sensor array with 20 × 20 mm^2 pixels by using $[C(NH_2)_3]ClO_4$-PU hybrid (**Figure 4**a). By virtue of its high sensitivity and excellent uniformity, the array is able to convert pressing, stretching, bending, shearing, and twisting mechanical load into a 2D voltage distribution map. As shown in Figure 4b–f, uniform voltage distribution is generated on the pixels under compression, while with stretching and bending, the high voltage regions appear in the middle and border of the array, respectively. For shearing, the voltage increases from one side to the other along the shearing force direction, and under the twisting mode, a twisted voltage geography is observed from the array. Our FEA simulations confirm the experimental results of the piezoelectric voltage maps generated by different loading modes (Figure S26, Supporting Information). We further demonstrate that a 3 × 4 sensor array based on $[C(NH_2)_3]ClO_4$-PU hybrid can be used to identify the movements of a robot wrist (e.g., listing, lowering, and twisting) (Figure S27, Supporting Information). Moreover, we have applied the array to monitor the loading conditions of the robot hand and to recognize the shape of objects (e.g., a tennis ball, a cell phone, and a stainless steel cup, Figure 4g–m) in the robot hand.

It is found that $[C(NH_2)_3]ClO_4$-PU hybrid is robust with high durability as no decay in the piezoelectric response has been observed with >3000 cycles of 2 kPa (10% strain) compressing, 5 kPa (10% strain) stretching, 100 kPa (7.5% strain) shearing, 0.06 N (1 mm displacement) bending, and 30° angle twisting, respectively (Figure S28, Supporting Information). Even after being subjected to pinching and kneading, $[C(NH_2)_3]ClO_4$-PU hybrid shows no decline in the piezoelectric response under a compression stress of 2 kPa (10% strain) (Figure S29, Supporting Information). Interestingly, marginal decay in the piezoelectric response was observed in the hybrid when measured at various humidity conditions from 40% to 90% humidity (Figure S30, Supporting Information).

One may concern that whether the two material phases, the molecular ferroelectric crystal and the PU skeleton, would slide with each other under mechanical loading. Based on our experimental observations and numerical simulations, we think such sliding is unlikely to occur. The mixing of these two phases is rather uniform and the molecular ferroelectric crystal is completely immersed into the skeleton (Figure 1g,h). Such a phase mixing occurs at submicron scale, making these two phases very coherent. This is different from two materials adjoined with a well-defined interface, for which interfacial sliding and delamination would occur under mechanical loading provided that the interfacial strength is low. Given such submicron-scale mixing, interfacial sliding is unlikely a dominant deformation mode, as the interface is enormous, and the energy required to activate the interfacial sliding must be tremendous. We thus believe that the mixture behaves as a homogenous composite material, and submicron scale sliding is unlikely to occur.

2.5. Scaling Analysis for Design

Upon compression, $[C(NH_2)_3]ClO_4$-PU hybrid undergoes three deformation stages,[48] the initial elastic (bending) stage, the buckling stage, and the condensation stage (Figure 3). A tiny load can bend the slender microbeams in the sponge, which is inherent to its ultrahigh sensitivity at the low-load regime (bending stage, ≤1 kPa). Beyond the bending stage, the microbeams in the sponge buckle and the sponge undergo large deformation but can hardly sustain any load increase. Within this regime, the stress in the microsponge saturates, suggesting that the piezoelectric sponge is no longer mechanosensitive to the pressure. However, as the buckling stage is very narrow within the stress range (Figure S19f, Supporting Information), the low sensitivity in this stage has little impact on the overall performance of $[C(NH_2)_3]ClO_4$-PU hybrid. In the condensation stage, almost all the microbeams are collapsed and start to contact with each other, corresponding to the rapid increase in the stiffness of the structure (Figure S19f, Supporting Information). $[C(NH_2)_3]ClO_4$-PU hybrid recovers its sensitivity to a high level to the applied load as the stress increases from 2.2 to 5 kPa.

The high sensitivity of the ferroelectric sponge sensors can be elucidated from a scaling analysis. For a typical open sponge structure, the characteristic dimensions of the constituent microskeletons are the length l and the cross-section area $A \sim t^2$. Here, we consider the ferroelectric sponge as a homogenous material with equivalent mechanical, piezoelectric, and dielectric properties, which will be hereafter denoted by symbols with a bar on the top. These structural equivalent properties will be compared with the intrinsic properties of the microskeletons with grafted ferroelectric crystals. The volume fraction of the skeletal material in the sponge is $V/\overline{V} = (t/l)^2 = \alpha$ and the relative mass density of the sponge is $\overline{\rho}/\rho = \alpha$, where $\overline{\rho}$ and ρ are the mass density of the sponge and the microbeams in the sponge, respectively. Similarly, $\overline{V}$ and V are the volume of sponge structure and that occupied by the microbeams in the sponge, respectively.

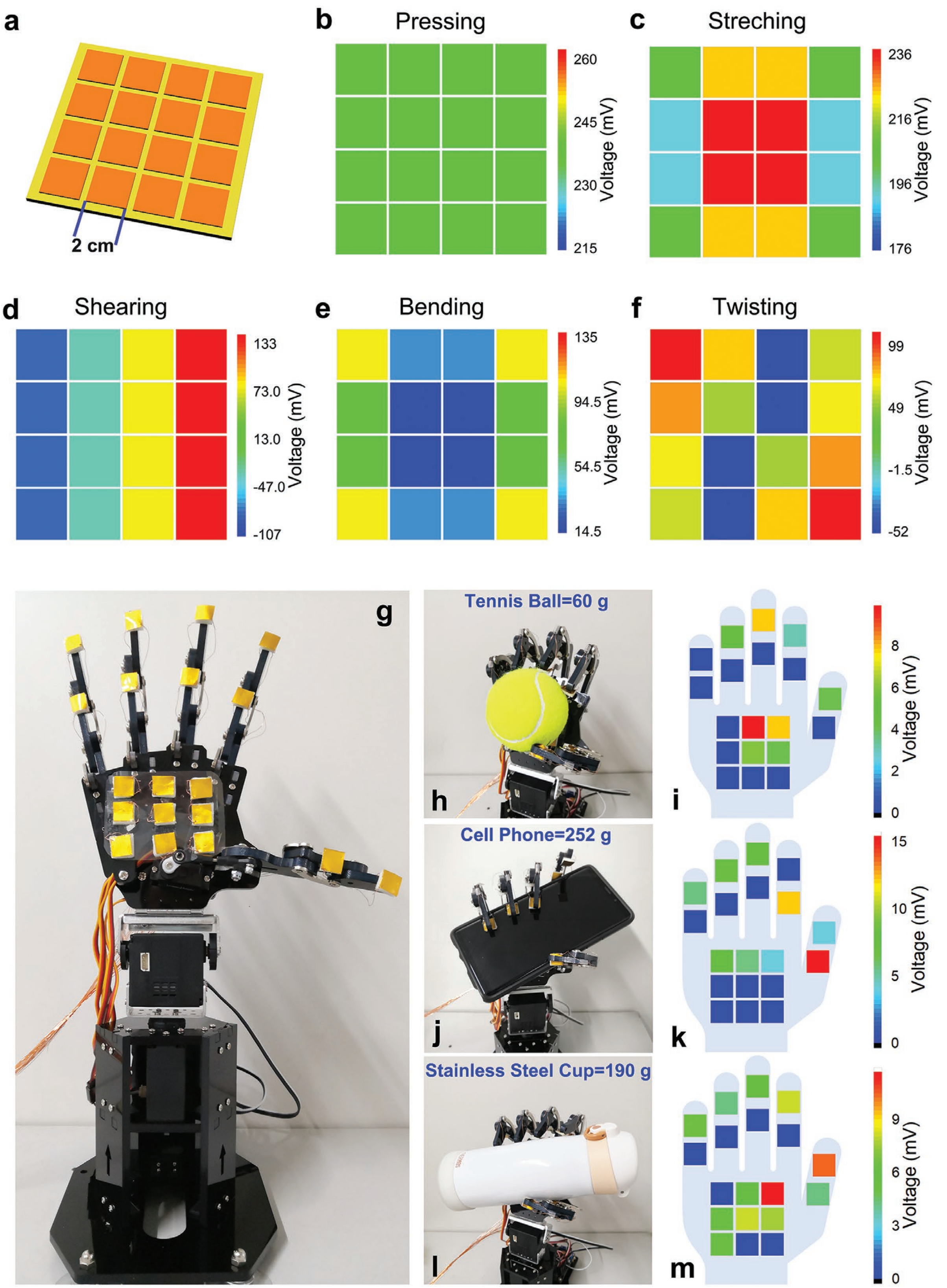

Figure 4. a) Schematic of the array. b–f) Voltage mapping of the array under pressing, stretching, bending, shearing, and twisting, respectively. g) The sensor array on a robot hand. h,j,l) The robot hand grasping different items, e.g., a tennis ball, a cell phone, and a stainless steel cup, respectively, i,k,m) the patterns on the hand can distinguish the items the hand grasping.

Under the external force F, the structural equivalent stress $\bar{\sigma} \sim F/l^2$ and the stress in the microbeams is to $\sigma = F/t^2$. Similarly, the equivalent strain is $\bar{\epsilon} \sim F/\bar{Y}l^2$, compared to the strain in the microbeams $\epsilon = F/Yt^2$ (Y represents the Young's modulus). Within the low-load regime, bending is the dominate deformation mode,[49] and the deflection due to bending is $\delta \sim Fl^3/YI \sim Fl^3/Yt^4$, where $I \sim t^4$ is the moment of inertia of the microbeam, the equivalent strain in the sponge is $\bar{\epsilon} = \delta/l = Fl^2/Yt^4$. The following scaling relations thus hold

$$\frac{\bar{\sigma}}{\sigma} \sim \alpha; \frac{\bar{\epsilon}}{\epsilon} \sim \alpha; \frac{\bar{Y}}{Y} \sim \alpha^2 \tag{1}$$

It should be noted that α^{-1} represents a stress-amplification factor. In the structural equivalent material, the stress is uniformly distributed, whereas when considering the microstructures the stress is only sustained by the thin microbeams, giving rise to the amplification factor.

The linear operation range of the ferroelectric sponge is limited by the buckling load of the microbeams. For Euler buckling, the onset buckling load is $F_{cr} = \pi^2 \bar{Y}I/l^2 \sim \bar{Y}d^4/l^2$. Considering the bending is the dominant deformation mode in the microbeam, the linear operation range of the sponge, denoted by the critical buckling stress $\bar{\sigma}_{cr}$, thus follows the following scaling relation

$$\frac{\bar{\sigma}_{cr}}{\bar{Y}} \sim \frac{F_{cr}/l^2}{\bar{Y}} = \frac{t^4}{l^4} = \alpha^2 \tag{2}$$

The generated polarization charges are $Q = P_e V$, where the dipole density is $P_e = d_{33}\ \sigma_{33}$. The same amount of polarization charges should be generated in the equivalent structures, i.e., $Q = \bar{d}_{33}\bar{\sigma}_{33}\bar{V}$. This gives rise to the ratio of the dielectric constants between the equivalent structures and the base material

$$\frac{\bar{d}_{33}}{d_{33}} \sim \frac{\sigma_{33}V}{\bar{\sigma}_{33}\bar{V}} \sim 1 \tag{3}$$

Similarly, the voltage generated by electric displacement is $\psi = (P_e/\varepsilon_{33})\ l = Ql/V\varepsilon_{33}$, the scaling of the dielectric constant can be written as

$$\frac{\bar{\varepsilon}_{33}}{\varepsilon_{33}} \sim \frac{V}{\bar{V}} \sim \alpha \tag{4}$$

Combining Equation (3) and Equation (4) yields

$$\frac{\bar{g}_{33}}{g_{33}} \sim \frac{\bar{d}_{33}}{d_{33}}\frac{\varepsilon_{33}}{\bar{\varepsilon}_{33}} \sim \alpha^{-1} \tag{5}$$

The scaling analysis reveals that the 3D interconnected structure of the hybrid plays a decisive role in the high performance, and the large porosity of the sponge amplifies the stress-amplification factor and leads to the small equivalent Young's modulus, resulting in the high piezoelectric sensitivity.

We have parameterized coupled constitutive relations (Note S1, Supporting Information) for the hybrid sponge from the microstructurally based simulations and elastomer mechanics theory,[50] which captures very well the nonlinear stress–strain relationships in the loading and unloading conditions (Figures S10b–e, S17, and S20b–e, Supporting Information). This constitutive relation allows us to simulate the hybrid sponge as continuum rather than discrete microbeams, thus significantly improving the computational efficiency. One notes that due to the complex deformation modes pertaining to the applied load, the microbeams in the sponge hence experience different deformation modes. The inhomogenous stress states correspond to the overall complex voltage generation in the piezoelectric sponge. Our simulation shows that pertaining to the three deformation stages (Figure S20a, Supporting Information). In the strain-stiffening and condensation stages, stress is continuously built into the microbeams, leading to rapid increases in the voltage. Whereas in the buckling stage, little stress is built in the microbeams due to the structural relaxation.

The scaling analysis predicts that the sensitivity of the sponge sensor scales with the relative density to the base material, $\bar{g}_{33} = \Lambda\alpha^{-1}$, where Λ is a constant and where $\alpha^{-1} = p/(1-p)$ and p is the porosity. We have chosen the same base material for sponges but different porosities, ranging from 95%, 96%, and 97% (**Figure 5**a). Our experimental measurements show the correspondent sensitivities are 170, 205, and 270 mV kPa^{-1}, corresponding to a linear coefficient of $\Lambda \cong 8.5$ (Figure 5b). An extrapolation to a porosity of 99%, the sensitivity would be close to 842 mV kPa^{-1}. On the other hand, the linear operation range of the sensors quadratically decays, manifested by the scaling relation of the buckling stress: $\bar{\sigma}_{cr} = \Gamma\alpha^2$. Our experimental measurements indicate $\Gamma = 930$. For a sponge with a porosity of 99%, $\bar{\sigma}_{cr} = 95$ Pa, as shown in Figure 5c. This shows that the enhancement of sensitivity by increasing the porosity compensates with decrease of the linear operation range (Figure 5c).

3. Conclusion

In conclusion, we present a facile and scalable approach to a new class of flexible piezoelectric sensor showing ultra-high sensitivity in the subtle pressure range. The key innovation of our material design is to utilize molecular ferroelectric as the active component that is fashioned into a 3D sponge structure to amplify the stress-amplification factor, endowing the resulting $[C(NH_2)_3]ClO_4$-PU hybrid with a small equivalent Young's modulus and a ultra-high piezoelectric sensitivity. $[C(NH_2)_3]ClO_4$-PU features a much lower detection limit with higher sensitivities when compared to the current piezoelectric sensors. By increasing the porosity of 3D microstructures of ferroelectric sponge, the sensitivity can be further improved as suggested by simulations and confirmed in the experimental studies. Our scaling analyses and simulations provide additional insights into the enhanced electromechanical coupling of the sponge structure and offer the design rules for improved sensitivity and flexibility of the ferroelectric sponges. Moreover, our flexible piezoelectric sensor exhibits a unique capability of sensing multimode mechanical forces from difference directions with excellent cyclic stability. Its superior capabilities are also demonstrated by monitoring the loading conditions and recognizing the shape of objects on the robot hand. This work provides a new paradigm for designing and applying molecular ferroelectric

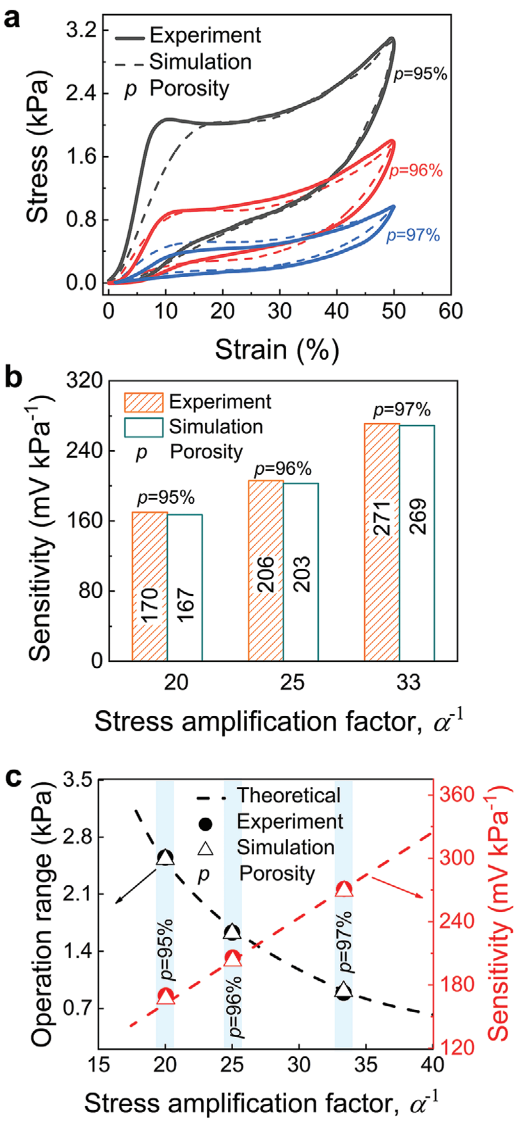

Figure 5. a) The experimental and FEA-simulated stress–strain curve of $[C(NH_2)_3]ClO_4$-PU hybrid with various porosity. b) The experimental and FEA-simulated sensitivities of $[C(NH_2)_3]ClO_4$-PU hybrid with different porosity and amplification factors (at the bending stage). c) The sensitivities (at the bending stage) and operation ranges of $[C(NH_2)_3]ClO_4$-PU hybrid with different porosity and amplification factors. Red line and symbols: sensitivity data. Black line and symbols: operation range data. Dashed line: theoretical prediction, solid circle: experimental measurements, hollow triangle: simulation results.

in technological applications and is anticipated to spur the advance of molecular ferroelectrics.

4. Experimental Section

Synthesis of Guanidinium Perchlorate ($[C(NH_2)_3]ClO_4$): The $[C(NH_2)_3]ClO_4$ crystal was obtained by evaporating the aqueous solution containing equal molar amounts of guanidinium carbonate (Aladdin, 99%) and perchloric acid (Sinopharm chemical reagent Co., Ltd., AR) at room temperature for few weeks. The synthesized $[C(NH_2)_3]ClO_4$ crystal was transparent and stable in the air. $[C(NH_2)_3]ClO_4$ could explode if heated at high temperatures >367 °C. It had a detonation velocity between 6000 and 7150 m s^{-1} for a specific gravity between 1.15 and 1.67. $[C(NH_2)_3]ClO_4$ should be kept in closed plastic bottles (http://www.sciencemadness.org/smwiki/index.php/Guanidinium_perchlorate).

Preparation of $[C(NH_2)_3]ClO_4$-PU Hybrids: The $[C(NH_2)_3]ClO_4$-PU hybrid sponge was fabricated by the simple soaking-drying method as illustrated in Figure S4, Supporting Information. The commercially available PU sponge (TX704, ITW Texwipe) was cut into the square with a volume of 20 × 20 × 3 mm^3 and washed by the deionized water and ethanol in turn. The 100 mg mL^{-1} of $[C(NH_2)_3]ClO_4$ solution was prepared by dissolving a certain amount of $[C(NH_2)_3]ClO_4$ crystal grains into deionized water. After stirring for 1 h, the cleaned PU sponges were immersed in the solution for several minutes to absorb the solution via capillary effect. The saturated PU sponge was squeezed and dried in the air at room temperature. The excessive solution was squeezed out and the remaining solution was wrapped over the whole sponge skeletons after squeezing. The $[C(NH_2)_3]ClO_4$ could naturally crystallize into the skeleton of sponge during the evaporation of remaining water. The $[C(NH_2)_3]ClO_4$-PU hybrid samples were then poled at room temperature with an electric field of 500 V mm^{-1} for 30 min.

Material Characterization: The phase information of the samples was confirmed by an XRD (7000S/L, Shimadzu Corp., Japan) with a Cu Kα radiation. The phase transition property of $[C(NH_2)_3]ClO_4$ crystal was obtained by a differential scanning calorimetry (STA449F3) at a heating rate of 5 °C min^{-1}. The microstructure of sponge and EDS of elements are recorded by a scanning electron micrograph (FESEM, Zeiss Geminisem 300). The piezoresponse force microscopy (PFM) was performed with an MFP-3D (Asylum Research, Santa Barbara, CA, USA). The polarization-electric field loops were tested by a Sawyer-Tower circuit (CPE1601, PolyK Technologies, State College, PA, USA). The dielectric properties of $[C(NH_2)_3]ClO_4$ crystal were measured via an impedance analyzer (Agilent 4294A; Agilent Technology Inc., Santa Clara, CA). The piezoelectric coefficients of $[C(NH_2)_3]ClO_4$ crystal were actual measured by a quasi-static d_{33}/d_{31} meter (Model ZJ-6A, Institute of Acoustics Academic Sinica). The mechanical characters of blank and hybrid sponge were performed with the BOSE 3220-AT testing machine (Type: Series II, Bose Corporation, Electro Force Systems Group, Eden Prairie, MN).

Fabrication of $[C(NH_2)_3]ClO_4$-PU Hybrid Sponge Sensors: Before fabricating the sensors, the $[C(NH_2)_3]ClO_4$-PU hybrid sponge was poled with a high voltage. Then single-sided conductive aluminum foils were used as the electrodes. Enameled copper wires with a diameter of 0.1 mm were connected to the electrodes using the silver paste, and the connecting junction was coated with ethyl α-cyanoacrylate glue. The electrodes were glued to the $[C(NH_2)_3]ClO_4$-PU hybrid sponge by ethyl α-cyanoacrylate glue to fabricate the final 3D network sensors. The carbon paste replaced the ethyl α-cyanoacrylate glue to connect the electrodes and hybrid sponge when carrying out the mechanical force tests with large deformation such as bending, stretching, and twisting. The regular electric signals were read out by the assembled testing circuit system, which consisted of a high resistance meter (Keithley, 6517B with an internal resistance of 200 TΩ and a sampling rate of 50, Figure S12, Supporting Information)[51] and a data acquisition system set up based on LabVIEW simulation model. The different objects including iron pillar (27 g), peanut (1.1 g), soybean (0.22 g), red bean (0.12 g), rice (0.024 g), and millet (0.0068 g) were used to verify the broad stress detection range by dropping them from a height of ~10 mm to upper surface of the hybrid sensors.

Construction of Array Signal Acquisition Circuit: Sensor array (4 × 4 pixels) was constructed to collect the electrical signals generating from the different mechanical force tests (Figure 3a). Each pixel had square electrodes with side length of 20 mm. The electrical signals were collected by a sampling system hardware including a control part and an ADC module part. The control part was implemented using a microcontroller STM32F407ZET6. The ADC module part (ADS1256) included a 24-bits high-resolution A/D converter chips. A 3 × 4 pixels sensor array with 12 square sensors (10 × 10 mm^2 of electrodes) was attached on the wrist of a mechanical palm to monitor the actual movements. Then 19 independent square sensors whose electrodes were 10 × 10 mm^2 were pasted on the different parts of the mechanical palm, which was used to grab different objects including tennis bale (60 g), cell phone (252 g), and stainless-steel cup (190 g) and aimed to extract character patterns from the output voltage signals.

Supporting Information

Supporting Information is available from the Wiley Online Library or from the author.

Acknowledgements

W.L. and C.L. contributed equally to this work. The authors acknowledge the support from the National Natural Science Foundation of China (grant nos. 51972126, 51972125, and 51772108), the Key Research and Development Project of Hubei Province (2020BAB067), and the Innovation Fund of WNLO and the Fundamental Research Funds for the Central Universities (2019KFYRCPY126). The authors also acknowledge the Analytical and Testing Center of Huazhong University of Science and Technology and Shanghai Strong Instruments Co., Ltd. for the help in experimental measurements.

Conflict of Interest

The authors declare no conflict of interest.

Data Availability Statement

The data that support the findings of this study are available from the corresponding author upon reasonable request.

Keywords

finite element analysis, flexible sensors, molecular ferroelectrics, multimodal stress detection, sensitivity

Received: May 29, 2021
Revised: July 19, 2021

---

[1] Y.-M. You, W.-Q. Liao, D. Zhao, H.-Y. Ye, Y. Zhang, Q. Zhou, X. Niu, J. Wang, P.-F. Li, D.-W. Fu, Z. Wang, S. Gao, K. Yang, J.-M. Liu, J. Li, Y. Yan, R.-G. Xiong, *Science* **2017**, *357*, 306.
[2] H.-Y. Zhang, X.-G. Chen, Z.-X. Zhang, X.-J. Song, T. Zhang, Q. Pan, Y. Zhang, R.-G. Xiong, *Adv. Mater.* **2020**, *32*, 2005213.
[3] D. Li, X.-M. Zhao, H.-X. Zhao, X.-W. Dong, L.-S. Long, L.-S. Zheng, *Adv. Mater.* **2018**, *30*, 1803716.
[4] L. Li, X. Liu, C. He, S. Wang, C. Ji, X. Zhang, Z. Sun, S. Zhao, M. Hong, J. Luo, *J. Am. Chem. Soc.* **2020**, *142*, 1159.
[5] J. Valasek, *Phys. Rev.* **1921**, *17*, 475.
[6] Y. Liu, B. Zhang, W. Xu, A. Haibibu, Z. Han, W. Lu, J. Bernholc, Q. Wang, *Nat. Mater.* **2020**, *19*, 1169.
[7] J. F. Scott, *Science* **2007**, *315*, 954.
[8] R. E. Newnham, L. J. Bowen, K. A. Klicker, L. E. Cross, *Mater. Des.* **1980**, *2*, 93.
[9] W. C. Goh, K. Yao, C. K. Ong, *Appl. Phys. A* **2005**, *81*, 1089.
[10] Y. Liu, Q. Wang, *Adv. Sci.* **2020**, *7*, 1902468.
[11] A. Chanthbouala, V. Garcia, R. O. Cherifi, K. Bouzehouane, S. Fusil, X. Moya, S. Xavier, H. Yamada, C. Deranlot, N. D. Mathur, M. Bibes, A. Barthélémy, J. Grollier, *Nat. Mater.* **2012**, *11*, 860.
[12] C. Dagdeviren, Y. Su, P. Joe, R. Yona, Y. Liu, Y.-S. Kim, Y. Huang, A. R. Damadoran, J. Xia, L. W. Martin, Y. Huang, J. A. Rogers, *Nat. Commun.* **2014**, *5*, 4496.
[13] H.-Y. Ye, Y.-Y. Tang, P.-F. Li, W.-Q. Liao, J.-X. Gao, X.-N. Hua, H. Cai, P.-P. Shi, Y.-M. You, R.-G. Xiong, *Science* **2018**, *361*, 151.
[14] Y.-Y. Tang, W.-Y. Zhang, P.-F. Li, H.-Y. Ye, Y.-M. You, R.-G. Xiong, *J. Am. Chem. Soc.* **2016**, *138*, 15784.
[15] W. Li, G. Tang, G. Zhang, H. M. Jafri, J. Zhou, D. Liu, Y. Liu, J. Wang, K. Jin, Y. Hu, H. Gu, Z. Wang, J. Hong, H. Huang, L.-Q. Chen, S. Jiang, Q. Wang, *Sci. Adv.* **2021**, *7*, eabe3068.
[16] W.-Q. Liao, D. Zhao, Y.-Y. Tang, Y. Zhang, P.-F. Li, P.-P. Shi, X.-G. Chen, Y.-M. You, R.-G. Xiong, *Science* **2019**, *363*, 1206.
[17] S. Wang, L. Li, W. Weng, C. Ji, X. Liu, Z. Sun, W. Lin, M. Hong, J. Luo, *J. Am. Chem. Soc.* **2020**, *142*, 55.
[18] A. Petritz, E. Karner-Petritz, T. Uemura, P. Schäffner, T. Araki, B. Stadlober, T. Sekitani, *Nat. Commun.* **2021**, *12*, 2399.
[19] S. Yang, J. Li, Y. Liu, M. Wang, L. Qiao, X. Gao, Y. Chang, H. Du, Z. Xu, S. Zhang, F. Li, *Nat. Commun.* **2021**, *12*, 1414.
[20] S. Xu, Y. Qin, C. Xu, Y. Wei, R. Yang, Z. L. Wang, *Nat. Nanotechnol.* **2010**, *5*, 366.
[21] Y.-C. Lai, J. Deng, R. Liu, Y.-C. Hsiao, S. L. Zhang, W. Peng, H.-M. Wu, X. Wang, Z. L. Wang, *Adv. Mater.* **2018**, *30*, 1801114.
[22] Y. Bai, H. Jantunen, J. Juuti, *Adv. Mater.* **2018**, *30*, 1707271.
[23] K. Song, R. Zhao, Z. L. Wang, Y. Yang, *Adv. Mater.* **2019**, *31*, 1902831.
[24] X. Gao, J. Wu, Y. Yu, Z. Chu, H. Shi, S. Dong, *Adv. Funct. Mater.* **2018**, *28*, 1706895.
[25] C. Baek, J. H. Yun, J. E. Wang, C. K. Jeong, K. J. Lee, K.-I. Park, D. K. Kim, *Nanoscale* **2016**, *8*, 17632.
[26] D. Y. Park, D. J. Joe, D. H. Kim, H. Park, J. H. Han, C. K. Jeong, H. Park, J. G. Park, B. Joung, K. J. Lee, *Adv. Mater.* **2017**, *29*, 1702308.
[27] L. Gu, J. Liu, N. Cui, Q. Xu, T. Du, L. Zhang, Z. Wang, C. Long, Y. Qin, *Nat. Commun.* **2020**, *11*, 1030.
[28] E. J. Lee, T. Y. Kim, S.-W. Kim, S. Jeong, Y. Choi, S. Y. Lee, *Energy Environ. Sci.* **2018**, *11*, 1425.
[29] Y. Zhang, C. K. Jeong, J. Wang, H. Sun, F. Li, G. Zhang, L.-Q. Chen, S. Zhang, W. Chen, Q. Wang, *Nano Energy* **2018**, *50*, 35.
[30] L. Lin, Y. Xie, S. Wang, W. Wu, S. Niu, X. Wen, Z. L. Wang, *ACS Nano* **2013**, *7*, 8266.
[31] F. Xu, Y. Zhu, *Adv. Mater.* **2012**, *24*, 5117.
[32] C. M. Boutry, M. Negre, M. Jorda, O. Vardoulis, A. Chortos, O. Khatib, Z. Bao, *Sci. Rob.* **2018**, *3*, eaau6914.
[33] Y. Luo, J. Shao, S. Chen, X. Chen, H. Tian, X. Li, L. Wang, D. Wang, B. Lu, *ACS Appl. Mater. Interfaces* **2019**, *11*, 17796.
[34] Z. Qiu, Y. Wan, W. Zhou, J. Yang, J. Yang, J. Huang, J. Zhang, Q. Liu, S. Huang, N. Bai, Z. Wu, W. Hong, H. Wang, C. F. Guo, *Adv. Funct. Mater.* **2018**, *28*, 1802343.
[35] G. Zhang, P. Zhao, X. Zhang, K. Han, T. Zhao, Y. Zhang, C. K. Jeong, S. Jiang, S. Zhang, Q. Wang, *Energy Environ. Sci.* **2018**, *11*, 2046.
[36] H. Cui, R. Hensleigh, D. Yao, D. Maurya, P. Kumar, M. G. Kang, S. Priya, X. Zheng, *Nat. Mater.* **2019**, *18*, 234.
[37] R. Hensleigh, H. Cui, Z. Xu, J. Massman, D. Yao, J. Berrigan, X. Zheng, *Nat. Electron.* **2020**, *3*, 216.
[38] Y. Zhang, C. K. Jeong, T. Yang, H. Sun, L. Chen, S. Zhang, W. Chen, Q. Wang, *J. Mater. Chem. A* **2018**, *6*, 14546.
[39] Z. Pajak, M. Grottel, A. E. Kozioł, *J. Chem. Soc., Faraday Trans. 2* **1982**, *78*, 1529.
[40] M. Szafrański, *J. Phys. Chem. B* **2011**, *115*, 8755.
[41] H. Guo, Y. J. Tan, G. Chen, Z. Wang, G. J. Susanto, H. H. See, Z. Yang, Z. W. Lim, L. Yang, B. C. K. Tee, *Nat. Commun.* **2020**, *11*, 5747.

[42] Y.-S. Kim, Y. Xie, X. Wen, S. Wang, S. J. Kim, H.-K. Song, Z. L. Wang, *Nano Energy* **2015**, *14*, 77.
[43] H.-J. Yoon, D.-M. Lee, Y.-J. Kim, S. Jeon, J.-H. Jung, S. S. Kwak, J. Kim, S. Kim, Y. Kim, S.-W. Kim, *Adv. Funct. Mater.* **2021**, *31*, 2100649.
[44] T. Q. Trung, N.-E. Lee, *Adv. Mater.* **2016**, *28*, 4338.
[45] Q. Jin, J. H. Lang, A. H. Slocum, *J. Microelectromech. Syst.* **2004**, *13*, 137.
[46] Z. Zhai, Y. Wang, H. Jiang, *Proc. Natl. Acad. Sci. U. S. A.* **2018**, *115*, 2032.
[47] D. Weaire, R. Phelan, *Philos. Mag. Lett.* **1994**, *69*, 107.
[48] L. J. Gibson, M. F. Ashby, *Proc. R. Soc., London, Ser. A* **1982**, *382*, 43.
[49] A. N. Gent, A. G. Thomas, *Rubber Chem. Technol.* **1963**, *36*, 597.
[50] R. W. Ogden, G. Saccomandi, I. Sgura, *Comput. Mech.* **2004**, *34*, 484.
[51] Q. Li, S. Li, D. Pisignano, L. Persano, Y. Yang, Y. Su, *Nano Energy* **2021**, *86*, 106045.